Stacking as a key property for creating nanoparticles with tunable shape: the case of squalenoyl-doxorubicin

Julie Mougin[1], Semen Yesylevskyy[2,4], Claudie Bourgaux[1], David Chapron[1], Jean-Philippe Michel[1], Franco Dosio[3], Barbara Stella[3], Christophe Ramseyer[4], Patrick Couvreur*[1]

[1]*Institut Galien Paris-Sud UMR CNRS 8612, Faculty of Pharmacy, Univ. Paris-Sud, Université Paris-Saclay, 92296 Châtenay-Malabry, France*

[2]*Department of Physics of Biological Systems, Institute of Physics of the National Academy of Sciences of Ukraine, Prospect Nauky 46, 03028 Kyiv, Ukraine*

[3]*Dipartimento di Scienza e Tecnologia del Farmaco, Università degli Studi di Torino, 10125 Turin, Italy*

[4]*Laboratoire Chrono Environnement UMR CNRS 6249, Université de Bourgogne Franche-Comté, 16 route de Gray, 25030 Besançon Cedex, France*

* To whom correspondence should be addressed: patrick.couvreur@u-psud.fr

ABSTRACT

The development of elongated nanoparticles for drug delivery is of growing interest in recent years, due to longer blood circulation and improved efficacy compared to spherical counterparts. Squalenoyl-doxorubicin (SQ-Dox) conjugate was previously shown to form elongated nanoparticles with improved therapeutic efficacy and decreased toxicity compared to free doxorubicin. By using experimental and computational techniques we demonstrate here that the unique physical properties of SQ-Dox, including stacking and electrostatic interactions of doxorubicin, as well as hydrophobic interactions of squalene, are involved in the formation of nanoassemblies with diverse elongated structures. We show that SQ-Dox concentration, ionic strength and anion nature can be used to modulate the shape and stiffness of SQ-Dox nanoparticles. As those parameters are involved into nanoparticles behavior in biological media, these findings could bring new opportunities for drug delivery and serve as an example for the design of new nanodrugs with stacking properties tuned for particular clinical purposes.

Doxorubicin (Dox) is a widely used anticancer drug presenting a broad spectrum of activity but limited by dose-dependent and irreversible cardiotoxicity.[1] To overcome this major drawback, we have previously conjugated the anticancer drug to squalene, a natural and biocompatible lipid, and it was found that the resulting bioconjugate was able to self-assemble into nanoparticles in water. This new nanomedicine displayed increased anticancer efficiency and decreased cardiotoxicity compared to free doxorubicin, which was attributed mainly to the elongated shape of the SQ-Dox nanoparticles.[2] Long flexible cylindrical micelles, generally referred to as wormlike micelles or filomicelles, have been first used for therapeutic purposes by Discher *and al.* in the middle of 2000's.[3,4] Interestingly, cylindrical paclitaxel-loaded polyethyleneglycol-polycaprolactone nanoparticles were observed to exhibit an extended circulation time in mouse bloodstream compared to analogous spherical particles, and a higher accumulation in xenograft tumors. Since then, increasing attention has been paid to the role of nanocarrier's shape for drug delivery. It has been revealed that beyond sustaining a long circulation time, elongated shape may favor margination (preferential migration of some nanoparticles close to the vessel wall in the bloodstream), allowing an improved delivery to target tissues via the Enhanced Permeation and Retention effect.[5] In addition, the nanoparticle rigidity may also impact the tumor accumulation: soft nanocarriers accumulate more in tumor tissues than the stiffer ones.[6,7] All these findings help considering wormlike nanoparticles as promising nanomedicines with a high degree of adjustability. As the majority of the efforts has been put on polymer wormlike nanoparticles in recent years[8–10], SQ-Dox is currently a unique simple non-polymeric nanomedicine forming elongated nanostructures with confirmed therapeutic efficacy.[11]

In the present study, it is discovered by which mechanism these elongated SQ-Dox nanoparticles form. The role of the added anion concentration and valency is also discussed, as a unique way to modulate the nanoparticle shape and rigidity. This could bring new opportunities in the drug delivery field by the design of nanomedicines with controlled shape and structure.

Structure of SQ-Dox nanoparticles

SQ-Dox nanoparticles were prepared by the nanoprecipitation of a THF solution of SQ-Dox hydrochloride in water, as previously described[2]. Clear red suspension of nanoparticles formed with a

ζ-potential of ~ +56 mV, arising from the positively charged ammonium group on the daunosamine sugar moiety of Dox. Cryo-TEM pictures of the 2 mM SQ-Dox nanoparticles suspension revealed the presence of small quasi-spherical nanoparticles with ~ 5-6 nm diameter, and only few long cylinders **(Fig. 1a)**. When increasing the concentration of SQ-Dox from 2 mM to 4 mM, cryo-TEM observations revealed the coexistence of short nanoparticles and wormlike nanoparticles with length up to microns **(Fig. 1b, Supplementary Fig. 1)**. A wormlike nanoparticle can be considered as a rigid rod on a small length scale defined as the persistence length l_p characterizing its flexibility.[12,13] In addition, some flexible nanoparticles of diameter ~ 5 nm seemed to assemble to form thicker ones of diameter ~ 11.7 nm. In general, it was observed that the number of long wormlike nanoparticles increased when raising SQ-Dox concentration.

Fig. 1c displays the small-angle X-ray scattering (SAXS) patterns of nanoparticle suspensions as a function of SQ-Dox concentration. The SAXS pattern of SQ-Dox suspensions at 2 mM concentration was modelled by core-shell prolate ellipsoids. The obtained lengths for short and long semi-axes were 2.3 nm and 3.4 nm, respectively, and the shell thickness was 1.1 nm, in good agreement with the size observed in cryo-TEM **(Fig. 1a)**. The SAXS patterns of more concentrated suspensions (4-15mM) were characteristic of cylindrical nanoparticles, as shown by the q^{-1} dependence of the scattered intensity I(q) at intermediate scattering vectors q ($q = 4\pi \sin\theta / \lambda$ where 2θ is the scattering angle and λ the X-ray wavelength).[14] In the high q region, short length scales were probed and the curves reflected the structure of the nanoparticle cross-section. The intermediate and high q regions of the curves could be well described with a model of core-shell cylindrical aggregate, the core and the shell corresponding to the hydrophobic SQ chains and the hydrophilic Dox polar heads, respectively **(Fig. 1d,e)**. Fitting of the SAXS curve resulted in a core radius of 2.2 nm, matching the length of stretched SQ chains, and a shell thickness of 1.1 nm. The fitting method is described in **Supplementary Information**.

The low q region contained information on the length and flexibility of the nanoparticles. Those features are expected to depend on the bioconjugate concentration. When the concentration increased, elongated nanoparticles tended to grow in order to minimize the excess of the free energy in

the system by reducing the number of end caps. Simultaneously, the rate of growth may be decreased by the electrostatic repulsions between charges along the nanoparticle body, favoring shorter nanoparticles.[12,13] The SAXS pattern of the 4 mM suspension could be fitted by ~ 18 nm-long cylinders. The increase in I(q) at lowest q values suggested the coexistence of these majority nanoparticles with long nanoassemblies. Upon ageing, short cylinders evolved toward long wormlike nanoparticles with 2lp ~ 40 nm, as shown by the SAXS curve recorded after 18 days **(Supplementary Fig. 2)**. For SQ-Dox concentration above 4 mM, the flattening in X-ray scattering intensity at low q and the broad maximum at about 0.24 nm^{-1}, indicative of a structure factor, emphasized the existence of repulsive interactions between nanoparticles, with an average distance between cylinders d ~ 26 nm. The interactions between nanoparticles depend on the effective volume fraction and dimensions of the nanoparticles. Due to the presence of charges, the diameter 2R of the nanoparticles was increased to the effective value $2R + 2\lambda_d$, where λ_d is the Debye screening length accounting for the extent of the electrostatic repulsion. The volume of a nanoparticle of length L was increased to the effective volume $\pi L(R + \lambda_d)^2$ **(Supplementary Table 2)**. Of note, the existence of interactions between nanoparticles is a major obstacle to determine their actual persistence length because the scattering in the low q region is affected by both the length of the nanoparticles and their interactions. Scattering in the intermediate q region provided the lower limit of the actual persistent (or nanoparticle) lengths (~ 13-20 nm).

The coexistence of rather short and long wormlike nanoparticles was further supported by the ultracentrifugation of the 8mM SQ-Dox suspension. The supernatant SAXS pattern could be modelled by rod-like particles with length ~ 20 nm, while the pellet pattern showed longer aggregated nanoparticles **(Supplementary Fig. 3)**.

The radial density distribution obtained from molecular dynamics (MD) calculations was in excellent agreement with these findings. **(Fig. 1f)** During the simulations **(Fig. 1d,e)**, spontaneous formation of cylindrical nanoparticles could be observed from initial unstructured SQ-Dox aggregates on the time scale of hundreds of nanoseconds **(Supplementary Fig. 4)**.

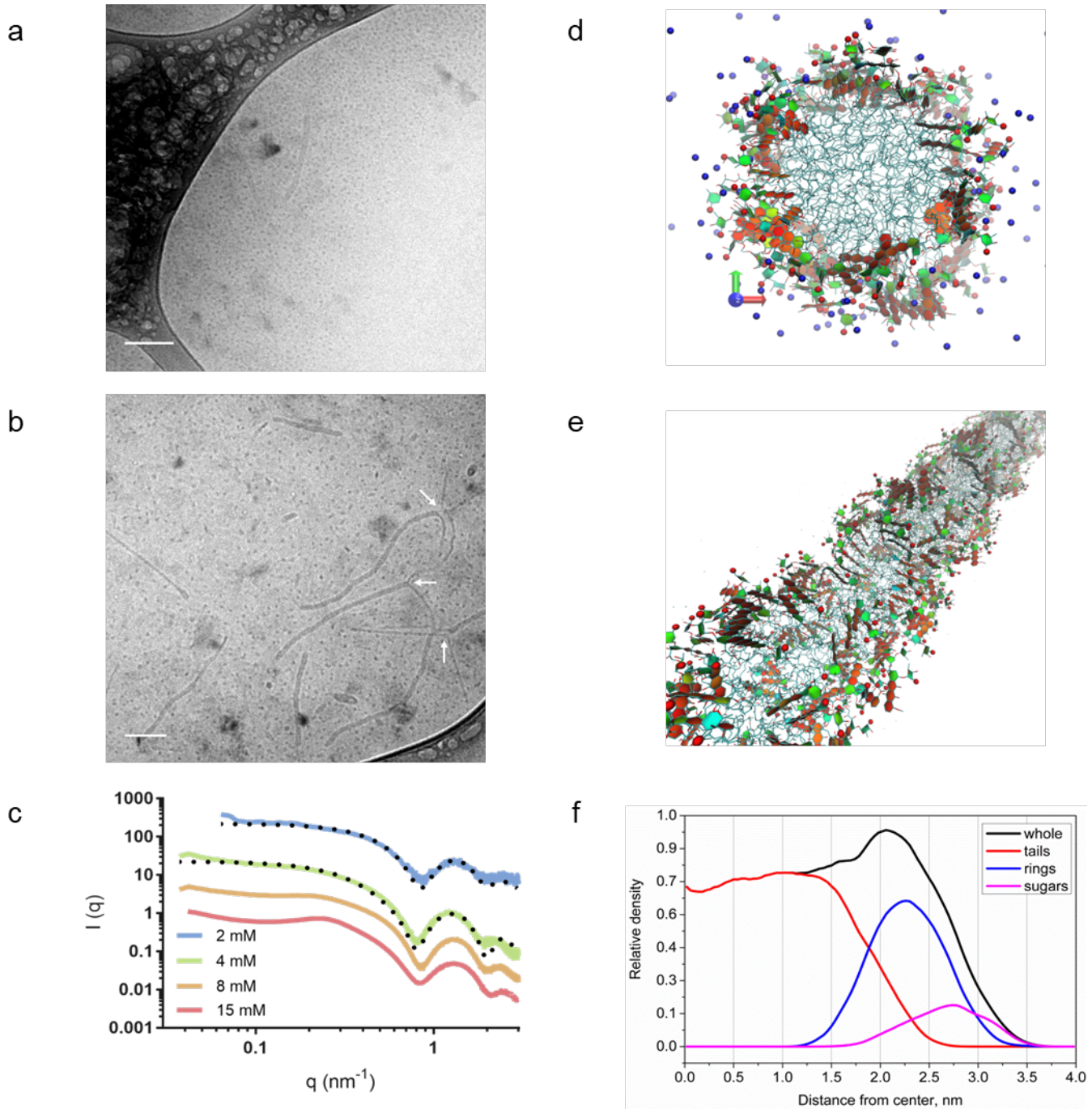

Figure 1: Structural characterization of SQ-Dox nanoparticles ***a.b.*** *Cryo-TEM micrographs of SQ-Dox nanoparticles suspensions prepared at* ***a.*** *2 mM (scale bar, 50 nm) and* ***b.*** *4 mM of SQ-Dox in water. The arrows indicate the interaction sites between SQ-Dox thin cylinders (scale bar, 100 nm).* ***c.*** *Small angle X-ray scattering pattern of SQ-Dox nanoparticles in water. The plain line represents experimental data and the dotted lines are the corresponding fits. Curves are shifted along the y-axis for clarity.* ***d.e.*** *Snapshots of a cylindrical NP. SQ tails are shown as sticks. Aromatic rings are filled with red and orange while non-aromatic rings are green and cyan. Positively charges NH_3^+ groups are shown as red spheres. Na^+ ions are blue spheres. Water is not shown for clarity.* ***d.*** *Front view.* ***e.*** *Perspective view.* ***f.*** *Radial density distribution (in dimensionless units) of the SQ chains and Dox heads in the cylindrical nanoparticle with Cl^- counter ions.*

Of note, the formation of cylindrical aggregates is specific to SQ-Dox and contrasts with the shape of other squalene-based nanoparticles.[15–18] We assume that it originates from Dox stacking.

Indeed, Dox is known to self-assemble in aqueous solution to form dimers, in parallel or antiparallel orientation, oligomers or fibers, depending on the concentration, the pH of the solution and the presence of added salts.[19–23] The absorbance and fluorescence spectra of SQ-Dox in water confirmed the stacking of Dox moieties in nanoparticles for concentration above 5 μM **(Supplementary Fig. 5)**.

In simulated SQ-Dox aggregates, the stacks started forming within hundreds of picoseconds and persisted on the time scales of hundreds of nanoseconds up to the end of the simulations. Four distinct types of stacks were observed, differing in the relative orientation of the Dox rings **(Fig. 2)**. The p-p stacks were the most abundant and tended to form extended fan-like structures, including up to six molecules with long axes slightly inclined to each other. Three subpopulations of p-p pairs, which differed in the inclination angle α and the distance d: p-p1 (d ~ 0.55 nm, α ~ 20°): p-p2 (d ~ 0.45 nm, α ~ 40°); p-p3 (d ~ 0.45 nm, α ~ 60°), coexisted in cylindrical nanoparticles **(Supplementary Fig. 6a)**. The free energy barrier of disrupting the p-p1 stacking interaction in cylindrical micelles was estimated in MD simulations as ~ 30 kJ/mol **(Supplementary Fig. 7)**. This indicated strong interaction with characteristic life time of minutes. a-a and p-a stacks were also observed while a-p stacks were very rare **(Supplementary Fig. 6b)**. Despite numerous subpopulations of stacked pairs, the orientation of Dox heads relatively to the radius of cylinders was rather homogeneous and formed a single dominant population **(Supplementary Fig. 6c)**. However, the relative abundances of the different types of stacks could not be quantified since the molecule stacking was correlated with the nanoparticle density, given in arbitrary units.

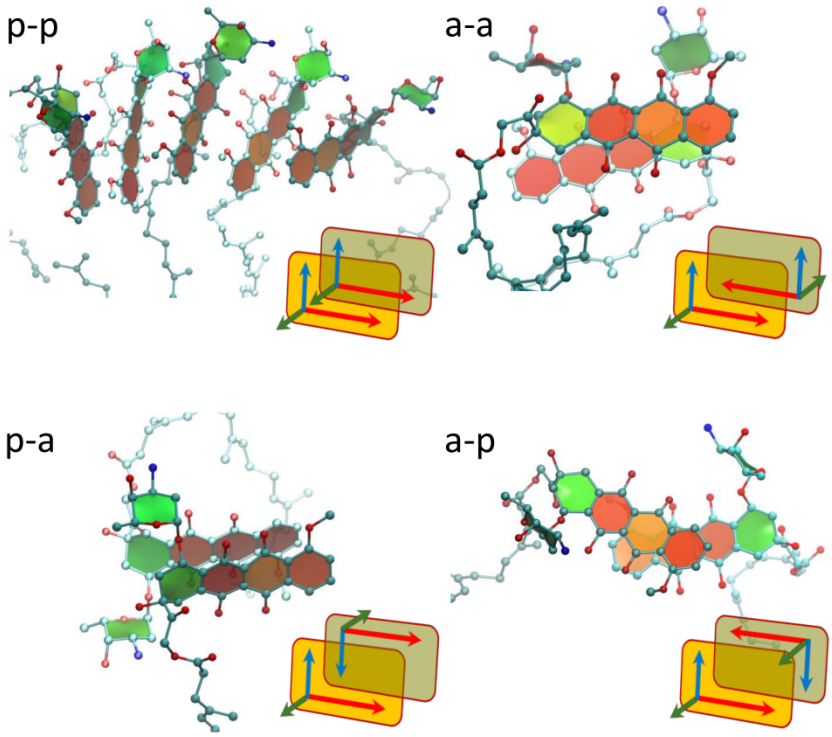

Figure 2: Different types of stacked aggregates observed in MD simulations. *Each panel shows a simulation snapshot with stacked SQ-Dox molecules in corresponding configuration and a scheme of the aggregate. On the scheme red, blue and green arrows correspond to long, short and normal axes of the Dox rings (see SI for details). Schemes are not aligned with the molecules on snapshots and correspond to them up to 3D rotation. On the first panel the fan-like aggregate of five stacked molecules in p-p orientation is shown. Other panels show aggregates of two molecules.*

To confirm the preferential assembling of SQ-Dox into cylindrical aggregates, the packing parameter p has been evaluated through Langmuir-Blodgett experiments. And a molecular area of 53 $Å^2$ was deduced from the SQ-Dox monolayer compression isotherm **(Supplementary Fig. 8a)**, leading to a p value of 0.51, clearly consistent with the formation of cylindrical nanoparticles.[24] The compressibility modulus K for the SQ-Dox monolayer exhibited a maximum value of 92 $mN.m^{-1}$, higher than the compressibility modulus maxima of squalenic acid and squalene-based cytidine derivatives, comprised in the 43-62 $mN.m^{-1}$ range **(Supplementary Fig. 8b)**.[25] This is likely a consequence of Dox stacking. Interestingly, this maximum was obtained for a large range of surface pressure, suggesting possible molecular reorganization in the monolayer.

Influence of salt on SQ-Dox nanoparticles structure

166 The influence of adding NaCl to an already prepared SQ-Dox nanoparticle suspension in water
167 was investigated, using a SQ-Dox:NaCl ratio of 1:1 mol:mol. Added salts are expected to screen the
168 intramicellar repulsive interactions between charges, entailing the growth of aggregates.[12] Cryo-TEM
169 pictures revealed that comparatively to SQ-Dox in pure water, the number and the length of long
170 wormlike nanoparticles increased after NaCl addition and the two previously described populations
171 with diameters ~ 5 nm and ~ 11.7 nm were detected **(Fig. 3a)**.

172 The SAXS pattern of a 2 mM SQ-Dox nano-suspension in the presence of 2 mM NaCl
173 revealed the formation of long wormlike nanoparticles **(Fig. 3b)**. The scattered intensity I(q) showed a
174 clear upturn in the low q region ($q \leq 0.25$ nm^{-1}) relative to the q^{-1} behavior typical of straight rods
175 observed at intermediate q values. In the 0.05-0.5 nm^{-1} q-range, the curve could be fitted with the two
176 models of long semi-flexible chains without interactions developed by Kholodenko and Pedersen and
177 Schurtenberger.[26,27] They yielded similar Kuhn lengths $2l_p \sim 30$ nm. For nanoparticles prepared at 4
178 mM and 8 mM, the repulsive interactions between the nanoparticles were screened upon addition of
179 NaCl, as shown by the disappearance of the correlation peak at $q \sim 0.24$ nm^{-1} compared to
180 nanoparticles in water **(Fig. 1d)** and by the q^{-1} dependence of the scattered intensity extending at low q
181 values **(Fig. 3b)**. The decrease of the Debye lengths λ_D also confirmed this screening process
182 **(Supplementary Table 2)**. The SAXS pattern of the 4 mM suspension could be fitted with a model of
183 100 nm-long stiff cylinders. Taken together, the above results suggested an increase of nanoparticle
184 flexibility with the addition of NaCl.

185 The screening of repulsive interactions between cylindrical aggregates may favor their side-
186 by-side association, as suggested by the scattering curve in the high q region of the SQ-Dox
187 nanoparticles at a concentration of 8 mM with NaCl at molar ratio 1:1 **(Fig. 3b)**. A factor structure,
188 resulting from the close packing of some cylinders, was superimposed on the oscillation at high q
189 while the low-q part of the curve could be fitted with 100 nm-long rods displaying an ellipsoidal cross-
190 section. The length of the short semi-axis and the ellipticity ratio were 3.8 nm and 2.2 respectively,
191 consistent with the size of the thicker nanoparticles. The peaks at 0.94 nm^{-1} and 1.7 nm^{-1} corresponded
192 to the first and second order of reflection arising from the stacking of cylinders with a mean distance
193 between their axes of ~ 6.7 nm, consistent with their diameter.

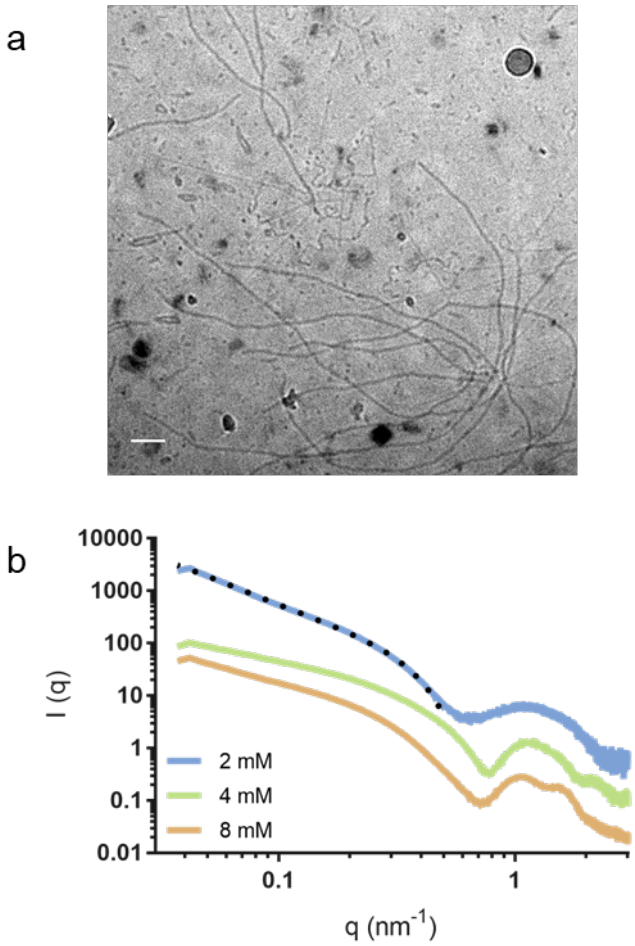

Figure 3: Morphological evolution of SQ-Dox nanoparticles. ***a.*** *Cryo-TEM micrograph of a suspension of nanoparticles prepared at a concentration of 2 mM in H_2O with addition of 2 mM NaCl (scale bar, 100 nm).* ***b.*** *Influence of salt addition on nanoparticles SAXS patterns. The SQ-Dox nanoparticles are prepared at concentrations ranging from 2 mM to 8 mM and NaCl is added using a molar ratio SQ-Dox:NaCl 1:1. The dotted line corresponds to the fit of the 2 mM curve. The curves have been shifted along the y-axis for clarity.*

Additional insights into the structure of the SQ-Dox nanoparticles were provided by AFM imaging. It has been observed that the AFM height image of the SQ-Dox samples displayed a mixture of spheres and long cylinders affected in two ways: (i) by the attractive interactions between the positively charged nanoparticles and the silicon surface that tended to flatten the nanoparticles and (ii) by the convolution between the AFM tip and nanoparticles lateral dimensions **(Fig. 4a)**. The AFM phase image suggested that thin cylinders formed helical bundles during their aggregation into thick cylinders **(see arrow in Fig. 4b)**. The MD simulations of interacting wormlike nanoparticles also highlighted the formation of twisted aggregates, which could also form helical bundles on larger scales **(Supplementary Fig. 9)**.

MD simulations also revealed the existence of inter-cylinder stacking interactions involving a-a and a-p stacking pairs. Although the formation of such "bridges" was rare (only two pairs were formed during the simulation time of 300 ns), they were able to keep the cylinders together once formed. This allowed us to hypothesize a "zipper-like" mechanism of interaction between the cylinders **(Fig. 4c)**. Once several inter-cylinder stacks formed, they would keep the cylinders at close distance for sufficiently long time to facilitate the formation of even more stacks. The formation of "zipped" cylinders was also clearly observed by cryo-TEM **(Fig. 4d).**

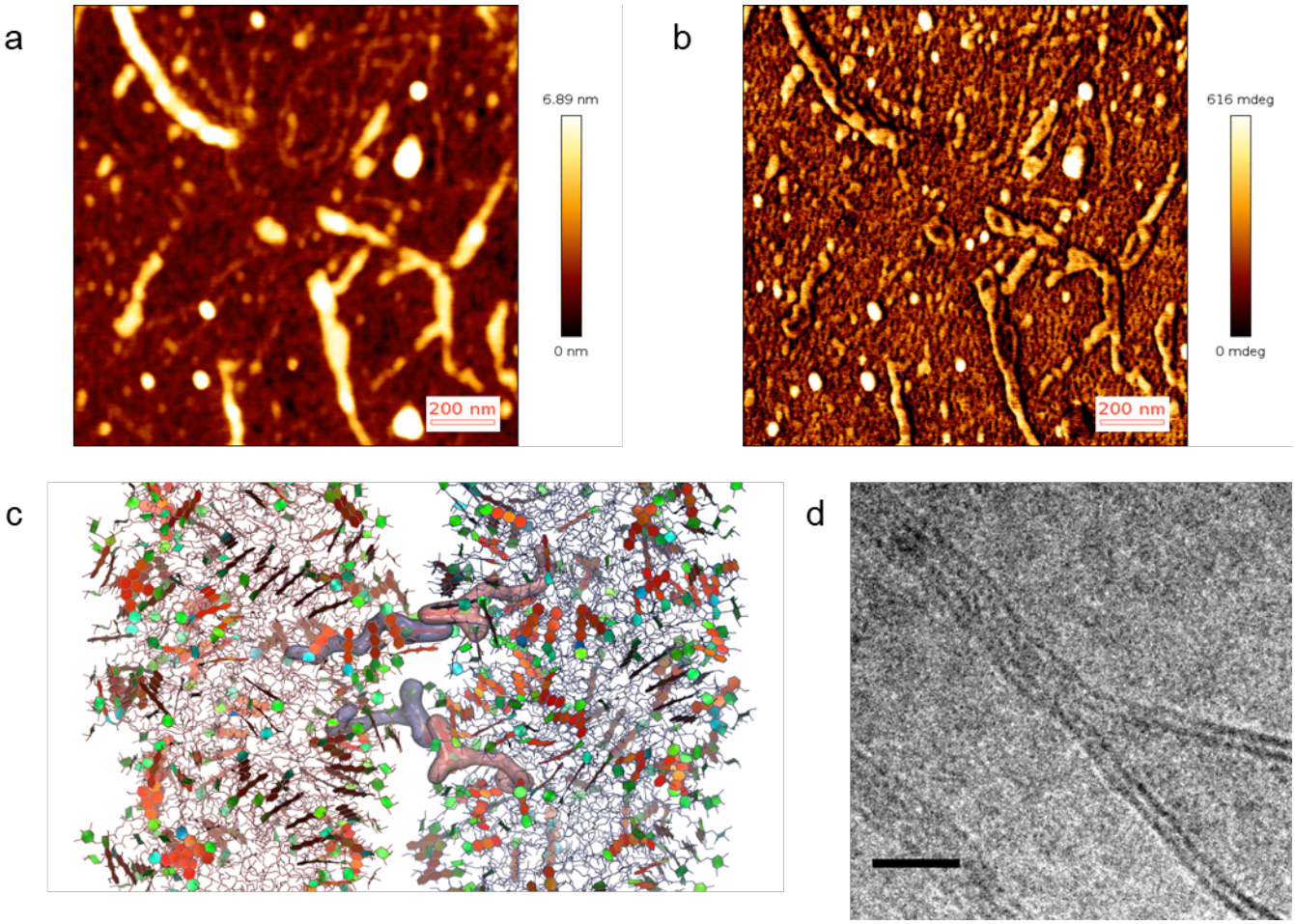

Figure 4: Mechanism of interaction between cylindrical nanoparticles with monovalent anions. ***a. b.*** *AFM pictures obtained in liquid medium of SQ-Dox nanoparticles (2 mM with 2 mM NaCl, scale bar, 200 nm).* ***a.*** *Height image.* ***b.*** *Phase image.* ***c.*** *MD simulations showing inter-cylinders stacking interactions. Stacking pairs from different cylinders are highlighted by semi-transparent surfaces. The colors are the same than in* ***Fig. 1****.* ***d.*** *Cryo-TEM pictures showing the stacking of SQ-Dox nanoparticles (2 mM with 2 mM NaCl) to form multilayer structures (Scale bar, 20 nm).*

Influence of the nature of the salt on the structures of the SQ-Dox nanoparticles

In order to investigate the impact of the nature of the salt on the supramolecular assembly of SQ-Dox, Na_2SO_4 was added to a 2 mM water suspension of nanoparticles, with addition of 0.01 to 1 mM Na_2SO_4 (SQ-Dox:Na_2SO_4 ratios 20:1 to 2:1 mol:mol, respectively). Using 0.01 mM Na_2SO_4, long core-shell cylinders were observed as the main population (**Fig 5a**) while with higher Na_2SO_4 concentrations, the divalent anions allowed the formation of wider (diameter ~ 14.3 nm, **Fig. 5b**, **Supplementary Fig. 10a**), shorter and more rigid cylindrical nanoparticles comparatively to monovalent anion (ie. NaCl). The SAXS curve at low q could be modeled by cylinders with a Lognormal distribution of radii around 7 nm, in agreement with the diameters measured in cryo-TEM experiment (**Fig 5a**). Both Cryo-TEM images and SAXS pattern suggested the formation of nanotubes consisting of an aqueous core surrounded by a SQ-Dox bilayer. Some images also suggested the existence of nanoassemblies comprising a SQ-Dox cylindrical core surrounded by a bilayer shell **(Supplementary Fig. 10b)**.

The possible formation of stable bilayers with an average thickness of ~ 4 nm was supported by MD simulation (**Fig 5c,d, Supplementary Fig. 11a,b**). Experimentally, the rod-to-bilayer transition was expected to arise from both the screening of charges and the ability of divalent anions to form long-lived bridges between charged Dox moieties. The distributions of the distances between N atoms of the sugar moieties in stacked Dox pairs were computed for Cl^- and SO_4^{2-} ions, demonstrating that these distances were significantly shorter in the presence of SO_4^{2-} ions **(Supplementary Fig 11c**). The decrease in electrostatic repulsion and salt bridges between nearest-neighbor amine groups led to a denser packing of SQ-Dox molecules, along with an increase in the packing parameter and a lower curvature of the nanoparticles. The bilayers thus formed were flexible enough to bend into cylinders.

Interestingly, some cryo-TEM images suggested the wrapping of a bilayer around a SQ-Dox cylinder **(Supplementary Fig. 10b)**. The formation mechanism could rely on the adsorption of SQ-Dox monomers at the surface of cylindrical nanoparticles through the formation of SO_4^{2-} bridges. The bilayer could then be generated by the addition of another layer of monomers to avoid unfavorable interaction of SQ chains with water. Tubes of 16-17 nm diameter, consisting in a SQ-Dox bilayer separated from the cylindrical core by a thin layer of water, were constructed in MD simulations

(**Supplementary Fig. 10c,d**). The density map of Dox headgroups in the cross-section, symmetrized radially around the axis of the tube, exhibited three distinct rings corresponding to the layers of Dox moieties located at distances of ~ 2.2 nm, ~ 4.1 nm and ~ 7.5 nm from the center. Those values are in good agreement with cryo-TEM observations **(Supplementary Fig. 10b,e)**.

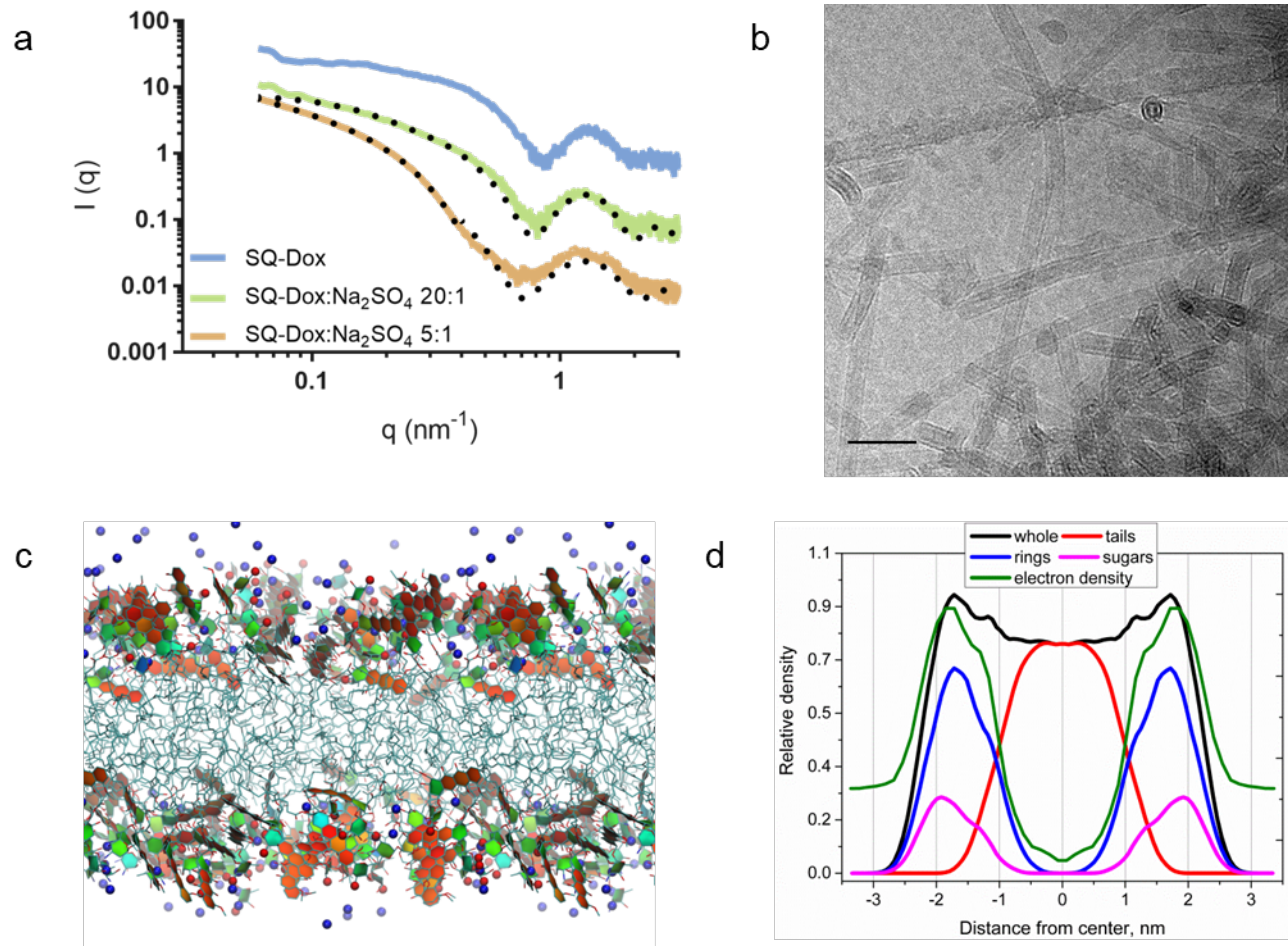

Figure 5: Morphology of SQ-Dox nanoparticles in the presence of divalent anions. ***a.*** *SAXS patterns of SQ-Dox nanoparticles in the presence of Na2SO4. The SQ-Dox nanoparticles are prepared at 2 mM and Na_2SO_4 is added at 0.01 mM (molar ratio 20:1) or 0.04 mM (molar ratio 5:1). The dotted lines correspond to the fits of the experimental curves. The curves have been shifted along the y-axis for clarity.* ***b.*** *Cryo-TEM micrograph of a suspension of SQ-Dox nanoparticles at a concentration of 2 mM with addition of 0.04 mM Na_2SO_4 (scale bar, 50 nm).* ***c.*** *Snapshot of equilibrated SQ-Dox bilayer. Squalene tails are shown as sticks. Aromatic rings are filled with red and orange while non-aromatic rings with green and cyan. Positively charged NH_3^+ group are shown as red sphere. Na^+ ions are blue. Water is not shown for clarity.* ***d.*** *Density profiles for equilibrated SQ-Dox bilayer including electron density profile.*

Discussion

SQ-Dox is a unique lipid-like molecule which combines stacking properties, ability to self-assemble as elongated nanoparticles in water and a demonstrated pharmacological activity, which

makes it appealing not only from the clinical perspective but also as a representative of a new class of self-assembling amphiphilic molecules with rich phase behavior. Stacking interactions of Dox heads not only lead to the formation of cylindrical nanoparticles instead of spherical, but such interactions also result in an impressive heterogeneity of nanoparticles surfaces, which contain four distinct topologies of stacks subdivided further into a number of sub-populations. The minor population of antiparallel stacks is especially important because of its ability to "zip" cylindrical nanoparticles together, leading to the formation of bundles and other complex aggregates, especially in the presence of salts. The charge of the Dox headgroups adds, indeed, another dimension for adjusting and controlling the nanoparticles structure. Higher concentrations of monovalent salts lead to the elongation of cylindrical nanoparticles, which could be beneficial for prolonging the blood circulation time and avoiding the capture by the macrophages of the reticule-endothelial system. But divalent anions provide another mechanism of cross-linking nanoparticles together by means of salt bridges, triggering a dramatic transition from individual cylindrical micelles to two-layer tubes in solutions on the late stages of their evolution. Suggested sequence of events during the evolution of SQ-Dox nanoparticles in different salt solutions is shown in **Fig. 6**.

Remarkably, the shape, size and surface properties of SQ-Dox nanoparticles could be modulated in broad ranges by varying the bioconjugate concentration, the ionic strength and the nature of the anion. But the present study also suggests that the nanoparticles in the test tube and in the body may not be the same since their structure may dramatically vary according to the local in vivo environment, and this may have some clinical implications. Nevertheless, SQ-Dox may serve as a model for creating new lipid-like self-assembling molecules with stacking and cross-linking behavior tuned for particular medical applications.

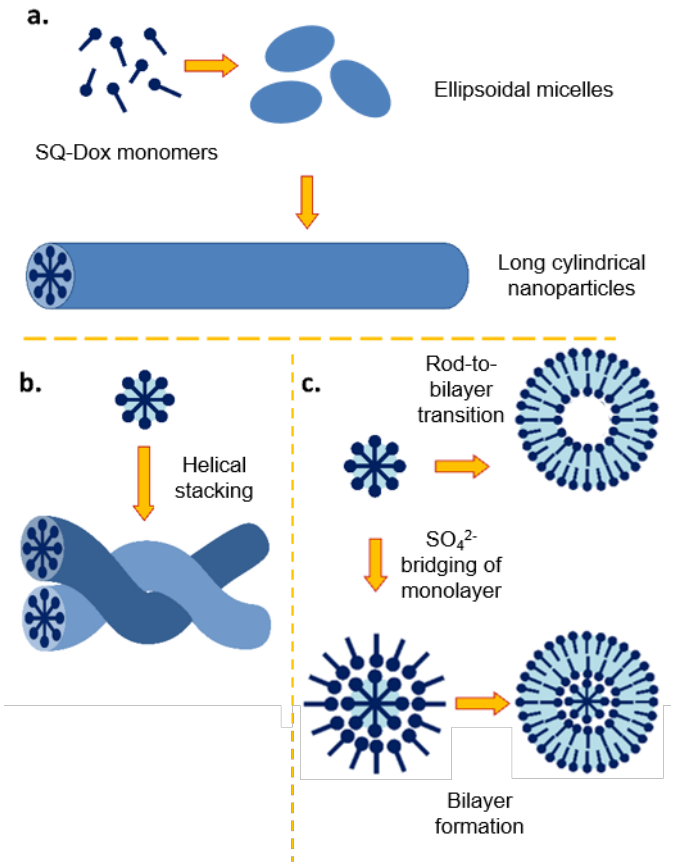

Figure 6: Schematic representation of the mechanisms of SQ-Dox assembly into elongated nanoparticles. ***a.*** *Early stages of assembly – spontaneous formation of short cylindrical micelles and their elongation.* ***b.*** *Late stages of assembly with monovalent anion.* **c.** *Late stages of assembly with divalent anions. Dox headgroups are shown as filled circles and squalene tails as rods. In panels* ***b.*** *and* ***c.*** *the hydrophobic areas are cyan while white areas are assumed to be filled with water.*

Methods

Formulation and characterization of SQ-Dox nanoparticles

SQ-Dox was synthesized as described in **Supplementary Information**. SQ-Dox nanoparticles were prepared according to the nanoprecipitation process, adapted from Maksimenko *and al.*[2] Practically, SQ-Dox (2 mg) was solubilized into 500 µL THF and added dropwise in 1 mL H_2O under stirring (500 rpm) using a syringe pump with a flow rate of 130 µL min. THF was then removed by evaporation at 20 °C under vacuum to obtain a suspension of SQ-Dox nanoparticles in water.

To study the influence of added salts, concentrated solutions were added to already prepared SQ-Dox nanoparticle suspensions. NaCl solutions were prepared at concentrations ranging from 200 to 800 mM. 2 µL of salt solution of appropriate concentration were added to 200 µL of SQ-Dox nanoparticles in water prepared at concentrations ranging from 2 mM to 8 mM, to reach a final SQ-Dox:NaCl molar ratio of 1:1. Na_2SO_4 solutions were prepared at concentrations ranging from 10 to 100 mM. 2 µL of salt solution of appropriate concentration were added to 200 µL of 2 mM SQ-Dox nanoparticles in water to reach a final SQ-Dox:Na_2SO_4 molar ratio ranging from 20:1 to 2:1.

The ζ-potential was measured at 25 °C after 1:10 dilution of SQ-Dox nanoparticles in 1mM NaCl solution using a Zetasizer Nano ZS (Malvern Panalyticals).

Cryo Transmission Electron Microscopy (Cryo-TEM)

5 µL of SQ-Dox nanoparticles at different concentrations (2 mM, 4 mM or 8 mM) in pure water or in the presence of salts (NaCl or Na_2SO_4 at molar ratios SQ-Dox:NaCl 1:1 or SQ-Dox:Na_2SO_4 20:1 to 2:1) were deposited onto a Lacey Formvar/carbon 300 Mesh Copper Grid (Ted Pella). The excess was manually blotted with a filter paper and the residual thin film was immediately frozen by plunging into liquid ethane cooled down at liquid nitrogen temperature using a Leica EM-CPC cryo-plunger. Observation was performed using a JEOL 2100HC microscope (JEOL Europe) or a JEOL 2200FS field emission microscope (JEOL USA) operating under an acceleration voltage of 200 kV in zero-loss mode (slit was 20 eV). High magnification images (2k by 2k pixels) were recorded by a CCD camera (Gatan Inc.) using Digital Micrograph software.

Atomic Force Microscopy (AFM)

SQ-Dox nanoparticles samples (2 mM) with or without NaCl (2 mM) were diluted 1:100 in water. 1 mL of this nanoparticles suspension was then deposited during 2 h onto a hydrophilic silicon surface previously treated with

acidic piranha solution. AFM experiments were performed using the Nanowizard 3 Ultra Speed (JPK Instruments), installed on an air-buffered table coupled to a dynamic anti-vibration device, and enclosed in an acoustic box. Imaging of the surface morphology was performed in air in AC mode with gold-coated silicon cantilever MLCT of 0.6 ± 0.1 N m^{-1} spring constant, 170 ± 5 kHz resonance frequency and 10 nm nominal radius of curvature (Bruker). The pyramid-shaped tips had a radius of curvature less than 20 nm. A free amplitude oscillation of 15 nm was chosen allowing the best resolution of the imaged surface. Setpoints ranging between 75% and 85% of the free amplitude were used. Images were taken at scan rate of 1 Hz. Image processing (flatten, plane fit, edge and hole detection) was performed with the JPK Data Processing software (JPK Instruments). At least three different areas of each sample were scanned and typical images were presented.

Small Angle X-Ray Scattering (SAXS)

SAXS experiments were performed on the SWING beamline at SOLEIL and on the BM29 beamline at ESRF. For measurements on the SWING beamline, samples were loaded into quartz capillaries (1.5 mm diameter). The scattering intensity I(q) was reported as a function of the scattering vector $q = 4\pi \sin\theta / \lambda$ where 2θ is the scattering angle and λ the X-ray wavelength. Data were recorded at 12 keV in the scattering vector q-range $0.04 < q < 4$ nm^{-1}, using a bi-dimensional Aviex detector. For each sample, 10 frames of 0.150 s were recorded at 20 °C and averaged. Water scattering was subtracted from the sample scattering. The beamline software Foxtrot was used for data collection and processing. On the BM29 beamline, samples were injected via an automated sample changer into a quartz capillary (1.8 mm internal diameter) and streamed at a constant flow rate through the capillary during beam exposure to avoid possible degradation under X-ray irradiation.[28] Data were recorded at 12.5 keV in the scattering vector q-range 0.04 < q < 5 nm-1, using a Pilatus 1M detector. For each sample 12 frames of 0.3 s were averaged and water scattering was measured before and after each sample.[29] The dedicated beamline software BsxCuBe was used for data collection and data processing was carried out using EDNA software.[30] For all of the samples, the scattering intensity was normalized with respect to the incident beam intensity, acquisition time and sample transmission. Structural information was retrieved from the SAXS patterns using the SASfit program.[31]

Molecular Dynamics force field

The topology of SQ-Dox was used from our previous study.[32] Initial topology of SQ-Dox was generated by Acpype topology generator.[33] The structure was optimized in Gaussian09[34] at the B3LYP/6-31++G(d) level of

theory. The ESP partial charges were computed and added to initial topology. The charges of topologically equivalent atoms were averaged. The charges of squalene moiety were set to zero except the linker between Dox and SQ. The atom types of squalene tails were adjusted to match lipids force field.

Construction of pre-arranged cylindrical aggregates

Cylindrical aggregates were also constructed from the pre-arrangement of SQ-Dox molecules in preferred orientation. This allowed much simpler simulation setup, which could be easily used to generate several initial structures for independent simulations. 100 SQ-Dox molecules were arranged into 10 disks with the molecules in each disk oriented radially around Z axis with Dox moiety facing outside. The system was solvated with ~13000 water molecules and either 100 Cl^- or 100 SO_4^{2-} and 50 Na^+ counter ions in such a way that the solvent did not penetrate into the region of the SQ tails. The system was equilibrated for 300 ns without any restraints.

Simulations of SQ-Dox bilayers

In order to simulate the bilayer phase of SQ-Dox, the molecules were arranged into the monolayer at 7x7 grid in XY plan with Dox moieties facing upwards. The second inverted monolayer was added and the system was solvated with ~ 5000 water molecules and the corresponding number of Cl^- counterions. No water molecules were placed into the region of SQ tails. The system was equilibrated for 300 ns without restraints. The area per molecule was used to monitor equilibration.

References

1. Lefrak, E. A., Piťha, J., Rosenheim, S. & Gottlieb, J. A. A clinicopathologic analysis of adriamycin cardiotoxicity. *Cancer* **32**, 302–314 (1973).
2. Maksimenko, A. *et al.* A unique squalenoylated and nonpegylated doxorubicin nanomedicine with systemic long-circulating properties and anticancer activity. *Proceedings of the National Academy of Sciences* **111**, E217–E226 (2014).
3. Geng, Y. *et al.* Shape effects of filaments versus spherical particles in flow and drug delivery. *Nature Nanotechnology* **2**, 249–255 (2007).

4. Christian, D. A. *et al.* Flexible Filaments for *in Vivo* Imaging and Delivery: Persistent Circulation of Filomicelles Opens the Dosage Window for Sustained Tumor Shrinkage. *Molecular Pharmaceutics* **6**, 1343–1352 (2009).
5. Li, Y. *et al.* Cell and nanoparticle transport in tumour microvasculature: the role of size, shape and surface functionality of nanoparticles. *Interface Focus* **6**, 20150086 (2016).
6. Champion, J. A. & Mitragotri, S. Shape Induced Inhibition of Phagocytosis of Polymer Particles. *Pharmaceutical Research* **26**, 244–249 (2009).
7. Sun, J. *et al.* Tunable Rigidity of (Polymeric Core)-(Lipid Shell) Nanoparticles for Regulated Cellular Uptake. *Advanced Materials* **27**, 1402–1407 (2015).
8. Jelonek, K., Li, S., Wu, X., Kasperczyk, J. & Marcinkowski, A. Self-assembled filomicelles prepared from polylactide/poly(ethylene glycol) block copolymers for anticancer drug delivery. *International Journal of Pharmaceutics* **485**, 357–364 (2015).
9. Wan, X. *et al.* Drug Combination Synergy in Worm-like Polymeric Micelles Improves Treatment Outcome for Small Cell and Non-Small Cell Lung Cancer. *ACS Nano* **12**, 2426–2439 (2018).
10. Nair, P. R. *et al.* Filomicelles from aromatic diblock copolymers increase paclitaxel-induced tumor cell death and aneuploidy compared with aliphatic copolymers. *Nanomedicine* **11**, 1551–1569 (2016).
11. Eksborg, S. Extraction of Daunorubicin and Doxorubicin and Their Hydroxyl Metabolites: Self-Association in Aqueous Solution. *Journal of Pharmaceutical Sciences* **67**, 782–785 (1978).
12. Dreiss, C. A. Wormlike micelles: where do we stand? Recent developments, linear rheology and scattering techniques. *Soft Matter* **3**, 956 (2007).
13. Lequeux, F. Structure and rheology of wormlike micelles. *Current Opinion in Colloid & Interface Science* **1**, 341–344 (1996).
14. Espinat, D. *Application des techniques de diffusion de la lumière, des rayons X et des neutrons à l'étude des systèmes colloïdaux*. (Technip, 1992).
15. Ralay-Ranaivo, B. *et al.* Novel self assembling nanoparticles for the oral administration of fondaparinux: Synthesis, characterization and in vivo evaluation. *Journal of Controlled Release* **194**, 323–331 (2014).

16. Hillaireau, H. *et al.* Anti-HIV efficacy and biodistribution of nucleoside reverse transcriptase inhibitors delivered as squalenoylated prodrug nanoassemblies. *Biomaterials* **34**, 4831–4838 (2013).
17. Gaudin, A. *et al.* Squalenoyl adenosine nanoparticles provide neuroprotection after stroke and spinal cord injury. *Nature Nanotechnology* **9**, 1054–1062 (2014).
18. Kotelevets, L. *et al.* A Squalene-Based Nanomedicine for Oral Treatment of Colon Cancer. *Cancer Research* **77**, 2964–2975 (2017).
19. Menozzi, M., Valentini, L., Vannini, E. & Arcamone, F. Self-Association of Doxorubicin and Related Compounds in Aqueous Solution. *Journal of Pharmaceutical Sciences* **73**, 766–770 (1984).
20. Agrawal, P., Barthwal, S. K. & Barthwal, R. Studies on self-aggregation of anthracycline drugs by restrained molecular dynamics approach using nuclear magnetic resonance spectroscopy supported by absorption, fluorescence, diffusion ordered spectroscopy and mass spectrometry. *European Journal of Medicinal Chemistry* **44**, 1437–1451 (2009).
21. Fülöp, Z., Gref, R. & Loftsson, T. A permeation method for detection of self-aggregation of doxorubicin in aqueous environment. *International Journal of Pharmaceutics* **454**, 559–561 (2013).
22. Li, X. *et al.* Doxorubicin physical state in solution and inside liposomes loaded via a pH gradient. *Biochimica et Biophysica Acta (BBA) - Biomembranes* **1415**, 23–40 (1998).
23. Zhu, L. *et al.* Fibril-shaped aggregates of doxorubicin with poly- L -lysine and its derivative. *Polym. Chem.* **5**, 5700–5706 (2014).
24. Israelachvili, J. & Ladyzhinski, I. The Physico-Chemical Basis of Self-Assembling Structures. in *Forces, Growth and Form in Soft Condensed Matter: At the Interface between Physics and Biology* (eds. Skjeltorp, A. T. & Belushkin, A. V.) **160**, 1–28 (Kluwer Academic Publishers, 2005).
25. Lepeltier, E. *et al.* Self-Assembly of Squalene-Based Nucleolipids: Relating the Chemical Structure of the Bioconjugates to the Architecture of the Nanoparticles. *Langmuir* **29**, 14795–14803 (2013).

26. Kholodenko, A. L. Analytical calculation of the scattering function for polymers of arbitrary flexibility using the Dirac propagator. *Macromolecules* **26**, 4179–4183 (1993).
27. Pedersen, J. S. & Schurtenberger, P. Scattering Functions of Semiflexible Polymers with and without Excluded Volume Effects. *Macromolecules* **29**, 7602–7612 (1996).
28. Round, A. *et al.* BioSAXS Sample Changer: a robotic sample changer for rapid and reliable high-throughput X-ray solution scattering experiments. *Acta Crystallographica Section D Biological Crystallography* **71**, 67–75 (2015).
29. Pernot, P. *et al.* Upgraded ESRF BM29 beamline for SAXS on macromolecules in solution. *Journal of Synchrotron Radiation* **20**, 660–664 (2013).
30. Brennich, M. E. *et al.* Online data analysis at the ESRF bioSAXS beamline, BM29. *Journal of Applied Crystallography* **49**, 203–212 (2016).
31. Breßler, I., Kohlbrecher, J. & Thünemann, A. F. *SASfit* : a tool for small-angle scattering data analysis using a library of analytical expressions. *Journal of Applied Crystallography* **48**, 1587–1598 (2015).
32. Yesylevskyy, S. O., Ramseyer, C., Savenko, M., Mura, S. & Couvreur, P. Low-Density Lipoproteins and Human Serum Albumin as Carriers of Squalenoylated Drugs: Insights from Molecular Simulations. *Molecular Pharmaceutics* **15**, 585–591 (2018).
33. Sousa da Silva, A. W. & Vranken, W. F. ACPYPE - AnteChamber PYthon Parser interfacE. *BMC Research Notes* **5**, 367 (2012).
34. Frisch, M. J. *et al. Gaussian 09*. (Gaussian, Inc.: Wallingford, CT, USA, 2009).

Acknowledgment

The authors thank ESRF and SOLEIL synchrotron facilities for the beamlines access. We also thank Ghislaine Frébourg (IFR 83 Biologie Intégrative, Paris, France), FRM 2006, SESAME 2005 and CNRS-ISB for providing access to JEOL 2100HC TEM, and Dr. Sylvain Trépout (Institut Curie, Orsay, France) and PICT-Ibisa for the experiments using JEOL 2200FS TEM. C.R. and S.Y. were supported by the European Union's Horizon 2020 research and innovation program under the Marie Sklodowska-Curie grant agreements No. 690853 and 796245,

474 respectively and the NATO grant SPS-G5291. The Centre de calcul regional Romeo and the Mésocentre de
475 calcul de Franche-Comté are deeply acknowledged for providing computational resources for this work.
476

477 **Author contributions**

478 P. C. designed the research. B. S. and F. D. performed the chemical synthesis of SQ-Dox. J. M. performed the
479 preparation of nanoparticles, the cryo-TEM observations, the Langmuir-Blodgett and spectroscopic experiments.
480 C. B. performed the SAXS experiments, analyzed the data and helped calculate the packing parameter. D. C.
481 helped to perform and to interpret the Langmuir-Blodgett experiments. J.-P. M. performed the AFM studies. S.
482 Y. and C. R. performed and analyzed the molecular dynamics simulations. J. M., S. Y. and C. R. wrote the
483 paper. All authors discussed the results and commented on the manuscript.
484

485 **Additional information**

486